

Multi-Scale Ionospheric Poynting Fluxes Using Ground and Space-Based Observations

D. D. Billett¹, K. A. McWilliams¹, P. V. Ponomarenko¹, C. J. Martin¹, D. J.
Knudsen², S. K. Vines³

¹Institute of Space and Atmospheric Studies, University of Saskatchewan, Saskatoon, SK, Canada

²Department of Physics and Astronomy, University of Calgary, Calgary, AB, Canada

³Johns Hopkins Applied Physics Laboratory, Laurel, MD, USA

Key Points:

- Filtered electric fields from the Swarm satellites agree exceptionally well with SuperDARN
- Variable and high-magnitude Poynting flux structures are embedded in and between field-aligned currents
- Poynting flux from sub-quasi-static dynamics can comprise as much as half of the total

Abstract

We present three events where high-resolution electric and magnetic field measurements from the Swarm satellite constellation coincided with excellent F-region ionospheric coverage from SuperDARN. Large-scale ionospheric convection patterns from SuperDARN, together with field-aligned-current patterns from AMPERE, provide information on quasi-static ionospheric dynamics traversed by Swarm. Because the Swarm observations and orbital path coincided with favorable SuperDARN/AMPERE observing conditions, it was possible to filter the Swarm electric field observations into a quasi-static component that agreed with the SuperDARN electric field. We contend that the residual electric field from Swarm is thus indicative of small- and mesoscale dynamics not captured by the convection and FAC patterns. We compare calculations of the Poynting flux between the different instruments and show that dynamics on small- to mesoscales can be highly variable within structures like field-aligned currents. In the events shown, small- and medium-scale Poynting fluxes occasionally dominate over that from large-scale processes.

Plain Language Summary

It is often thought that a significant amount of space weather energy deposited into the upper atmosphere of Earth (above ~ 100 km altitude) is contained within small-scale (on the order of kilometres) fluctuations of the electric field. This kind of variability is difficult to measure due to the sparse resolution (both in space and time) of instruments like ground-based instruments, or the global fitting procedures of satellite constellations. Those instruments, which tend to focus on observing large-scale “big picture” dynamics, do however excel at providing important information about the global state of the upper atmosphere. We use small-scale (~ 1 km) data from the Swarm satellites in this letter, in conjunction with ground-based radars and a satellite constellation, to obtain a complete picture of how space weather energy dissipation is spread across all scale sizes. We find that small features that only Swarm can see occasionally dominate in terms of energy balance.

1 Introduction

Electric and magnetic fields in the high-latitude ionosphere have been studied for decades as measures of space-weather/atmosphere coupling. At large scales, on the order of thousands of kilometres, Dungey cycle convection of the magnetosphere drives field-

aligned currents (FACs) and ionospheric plasma convection (Dungey, 1961; Iijima & Potemra, 1976; Cowley & Lockwood, 1992; Weimer, 2001). These “quasi-static” or “DC” processes are typically well characterised by statistical datasets as being controlled by the orientation of the interplanetary magnetic field (e.g. Heppner & Maynard, 1987; Ruohoniemi & Greenwald, 1996). However, there are strong modes of spatial and temporal variability at small- and mesoscales that are difficult to model (Cousins et al., 2013). Causes of sub-quasi-static variability are wide ranging (Yu et al., 2022), and include processes such as substorms (Grocott et al., 2009; Zou et al., 2009), particle precipitation (Senior et al., 2002; Billett et al., 2020), and sub-auroral polarisation streams (SAPS; Clausen et al., 2012; Billett, McWilliams, Kerr, et al., 2022). On the order of kilometres, kinetic Alfvén waves drive a large degree of small-scale variability (Lühr et al., 2015).

Large-scale dynamics of the high-latitude ionosphere are notoriously difficult to decouple from small- and mesoscale dynamics. Ground-based instruments, such as incoherent and coherent scatter radars, magnetometers, and ionosondes, for example, excel at observing large-scale quasi-static structures due to consistently observing a specific region of space. Satellites, on the other hand, can measure ionospheric electric and magnetic fields at a very high cadence in-situ, but cannot distinguish between spatial and temporal variations. It is often challenging to scrutinise high-resolution satellite measurements without fully being aware of the underlying quasi-static dynamics that are being traversed, such as large-scale Birkeland/FACs, convective flows, and auroral arcs. Whilst one might think that the quasi-static system is responsible for most of the electromagnetic energy being transferred between the magnetosphere and atmosphere (otherwise known as the Poynting flux), there is in fact a much more complicated and poorly understood balance of that energy across all spatial scales (Codrescu et al., 1995; Y. Deng & Ridley, 2007; Keiling et al., 2019). For example, recent work from Billett, McWilliams, Pakhotin, et al. (2022) estimated that the observed Poynting flux drops off rapidly when low-pass filtering high-resolution measurements from 1 km to 15 km, and then drops off linearly to a $\sim 50\%$ underestimation at around 1000 km scale size (relative to 1 km scale sizes). Because no single instrument can fully capture the complex cross-scale dynamics that leads to this energy discrepancy, conjunctions between ground and space-based instrumentation are actively sought after, with the former often being referred to as providing a vital spatially extensive region of context for spacecraft observations without which the latter would be considerably less informative.

In this letter, we present multi-scale observations of the high-latitude ionosphere using data from the Swarm satellite constellation, the Super Dual Auroral Radar Network (SuperDARN), and the Active Magnetosphere and Planetary Response Experiment (AMPERE). SuperDARN and AMPERE datasets provide global-scale maps of the ionospheric quasi-static electric and perturbation magnetic fields, respectively, whilst instruments on-board Swarm capture small and mesoscale variability. We extract the residual variability in the Swarm data that is not captured by the large scale, quasi-static SuperDARN and AMPERE measurements. We compare quasi-static and residual Poynting fluxes, revealing strong multi-scale structuring and variability embedded within the large-scale FACs.

2 Data

2.1 Swarm

16 Hz ion velocities and 50 Hz magnetic fields from Swarm A and B, at polar orbit altitudes of ~ 460 km and ~ 510 km, respectively, are obtained from the Thermal Ion Imager (TII; Knudsen et al., 2017) and Vector Field Magnetometer (VFM; Leger et al., 2009) instruments. VFM data is downsampled to 16 Hz by averaging for the purpose of this study, to remain consistent with the TII and for the proceeding processing steps. “Spikey” noise in the ion drift data, defined as a single timestep where the velocity has a difference 300 m s^{-1} greater than both its neighbours, is corrected with the mean of its neighbours.

The Swarm electric field (\mathbf{E}) is derived from the ion velocity (\mathbf{v}) and magnetic field \mathbf{B} through the relationship $\mathbf{E} = -\mathbf{v} \times \mathbf{B}$. We then employ a filtering scheme in order to separate the large-scale quasi-static system from the total electric field. A 225s Savitsky-Golay low-pass filter, as used in previous studies of Swarm derived Poynting flux (Ivarsen et al., 2020; Billett, McWilliams, Pakhotin, et al., 2022), produces this quasi-static electric field component ($\mathbf{E}_{\text{static}}$) and leaves a residual ($\delta\mathbf{E}$). After subtracting the terrestrial background field from the Swarm magnetic field using the International Geomagnetic Reference Field (IGRF; Alken et al., 2021) to get the perturbation ($\delta\mathbf{B}$), a “quasi-static” and “residual” Poynting flux can be derived:

$$\mathbf{S}_{\text{static}} = -\frac{1}{\mu_0} (\mathbf{E}_{\text{static}} \times \delta\mathbf{B}) \cdot \hat{B} \quad (1)$$

$$\mathbf{S}_{\text{residual}} = -\frac{1}{\mu_0} (\delta\mathbf{E} \times \delta\mathbf{B}) \cdot \hat{B} \quad (2)$$

where μ_0 is the permeability of free space and \hat{B} is a unit vector in the magnetic field direction. Assuming variations in \mathbf{E} and \mathbf{B} are mostly horizontal, the Poynting fluxes derived from Equations 1 and 2 are completely in the magnetic field-aligned direction. Thus, the Swarm \mathbf{E} and \mathbf{B} data are additionally transformed into mean field-aligned (MFA) coordinates (magnetic north, east, and field-aligned) from satellite track orientated (along-track, cross-track, and vertical) prior to calculating the Poynting fluxes.

2.2 SuperDARN and AMPERE

SuperDARN (Greenwald et al., 1995) consists of multiple high-frequency ground-based radars in both the northern and southern mid to high latitudes. Each radar measures the line-of-sight plasma velocity in the ionosphere by calculating the Doppler shift of high-frequency signals scattered by field-aligned electron density irregularities. At high-latitudes this plasma velocity mainly corresponds to the F-region convective ion-drift imposed on the ionosphere by the magnetospheric Dungey cycle, but could also be a result of mesoscale processes such as travelling ionospheric disturbances and MHD waves. When line-of-sight velocity vectors from multiple SuperDARN radars are combined, a large-scale fit can be carried out to solve for the high-latitude electric potential (Φ) in a given hemisphere (Ruohoniemi & Baker, 1998). Utilizing the relationships $\mathbf{E} = -\nabla\Phi$ and $\mathbf{v} = (\mathbf{E} \times \mathbf{B})/B^2$, the contours of Φ relate directly to the ionospheric convection velocity and electric field. We utilize northern hemisphere SuperDARN convection patterns in this letter, supplemented with an empirical model based on the statistical dependence of SuperDARN convection patterns to the interplanetary magnetic field (Thomas & Shepherd, 2018), to fill gaps in radar coverage. The integration time for a single convection map is nominally 2 minutes.

AMPERE (Anderson et al., 2014, 2021) provides global scale measurements of magnetic fields perturbed ($\delta\mathbf{B}$) due to FACs. These are obtained from the Iridium Communications Satellite Network constellation after subtracting the background terrestrial magnetic field from onboard magnetometer data using a main field reference model (IGRF or the World Magnetic Model (WMM; Chulliat et al., 2020)), then fitting a spherical harmonic formulation (Waters et al., 2001, 2020). The $\delta\mathbf{B}$'s are related to the FAC densities, \mathbf{J} , by $\nabla \times \delta\mathbf{B} = \mu_0 \mathbf{J}$. AMPERE fitted $\delta\mathbf{B}$'s and FAC's are produced at a 10 minute integration and 2 minute cadence. These fitted AMPERE data products are sampled onto a 1° magnetic latitude by 1 hour of magnetic local time (MLT) grid.

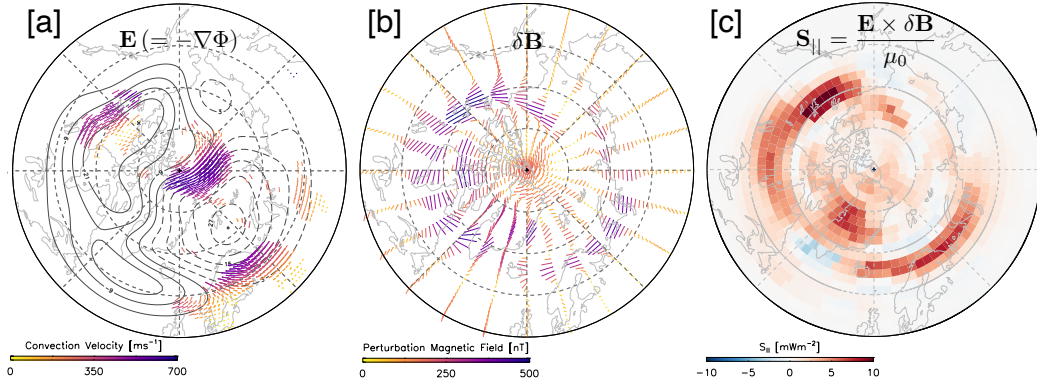


Figure 1. Example northern hemisphere Poynting flux calculation for 2013-10-14, 14:00 UT. [a] SuperDARN electric potential convection pattern with the locations of binned radar data colored as velocity vectors. [b] AMPERE perturbation magnetic fields. [c] Equivalent Poynting flux calculated on the same grid as AMPERE using [a] and [b]. The coordinate system is Altitude Adjusted Corrected Geomagnetic (AACGM Shepherd, 2014) latitude and local time, in a polar plot format with noon at the top and dawn to the right. The plot extends to 50 degrees AACGM latitude in 10 degree segments.

By using the global fits to \mathbf{E} and $\delta\mathbf{B}$ from the SuperDARN and AMPERE, the Poynting flux can be derived globally using equation 1 (Waters et al., 2004; Billett et al., 2021; Billett, McWilliams, Perry, et al., 2022). Figure 1 shows an example SuperDARN/AMPERE Poynting flux calculation, illustrating that it is a powerful technique to achieve a data-driven snapshot of the global Poynting flux morphology. Given that both the SuperDARN and AMPERE in this instance utilize fits which significantly smooth out spatiotemporal fluctuations in the ionospheric electric and magnetic fields, we treat the resulting Poynting flux as essentially quasi-static only.

We additionally note that because the Iridium satellites orbit at a high F-region altitude of ~ 780 km, a correction for the curvature of the magnetic field is applied to the AMPERE $\delta\mathbf{B}$'s to project them to an altitude of 250 km (approximately the SuperDARN backscatter altitude, using the 3/2 relationship described by Knipp et al. (2014)). The same correction procedure is applied to the Swarm data.

2.3 Event Selection

We note here that the Swarm along-track ion velocities from the TII sensors contain significant errors (Lomidze et al., 2019) associated with variations in the satellite floating potential (Burchill & Knudsen, 2016). We therefore impose a strict selection criterion for the events shown in this letter, to times where we expect the along-track ion-velocity to be small so that it can be set to zero. Because $\mathbf{E} = -\mathbf{v} \times \mathbf{B}$, the along-track ion-drift errors would propagate into the derived cross-track electric field. We thus utilize the SuperDARN plasma convection patterns, on an event-by-event basis, to find occurrences of when the Swarm orbital trajectory was parallel to the electric field (i.e., when along-track is aligned with the electric field) for extended periods of time. An example of when this scenario would happen is during a cross-polar-cap satellite pass which directly bisects a plasma convection cell, perpendicular to the ion-drift. This is of course not a perfect solution, because we expect that SuperDARN convection patterns are poor at capturing variability much smaller than quasi-static scale sizes. However, it minimizes avoidable errors in the Swarm electric field for the purpose of comparisons with SuperDARN convection patterns. Previous studies have carried out comprehensive validations of the ion-drifts from Swarm, including comparisons with those from the SuperDARN (Fiori et al., 2016; Lomidze et al., 2019; Koustov et al., 2019; Burchill & Knudsen, 2022).

Supplementary criteria for identifying “good” Swarm-SuperDARN-AMPERE conjunction events are more adaptable. Foremost is that there should be excellent SuperDARN data coverage in the region a Swarm satellite is flying over, using a preliminary binned vector threshold of 500 points for the whole map, to ensure the electric potential convection fit is well constrained. Secondly, both the SuperDARN convection and AMPERE FAC patterns should reasonably agree with each other, because we expect the convection and FAC boundary positions to have a linear relationship (Clausen et al., 2013; Fogg et al., 2020). In practical terms, the high-latitude R1 FACs should approximately extend through the centre of the convection cell, whilst the lower latitude R2 FACs should lie slightly poleward of the Heppner-Maynard boundary. Discontinuity between a SuperDARN convection and AMPERE FAC pattern could be due to poor SuperDARN data coverage, or particularly harsh horizontal conductivity gradients (Sofko et al., 1995). However, the along-track electric field and SuperDARN data threshold criteria described above reduces the number of Swarm-SuperDARN-AMPERE northern hemisphere conjunction events significantly. Thus, the events were checked by hand for good convection/FAC

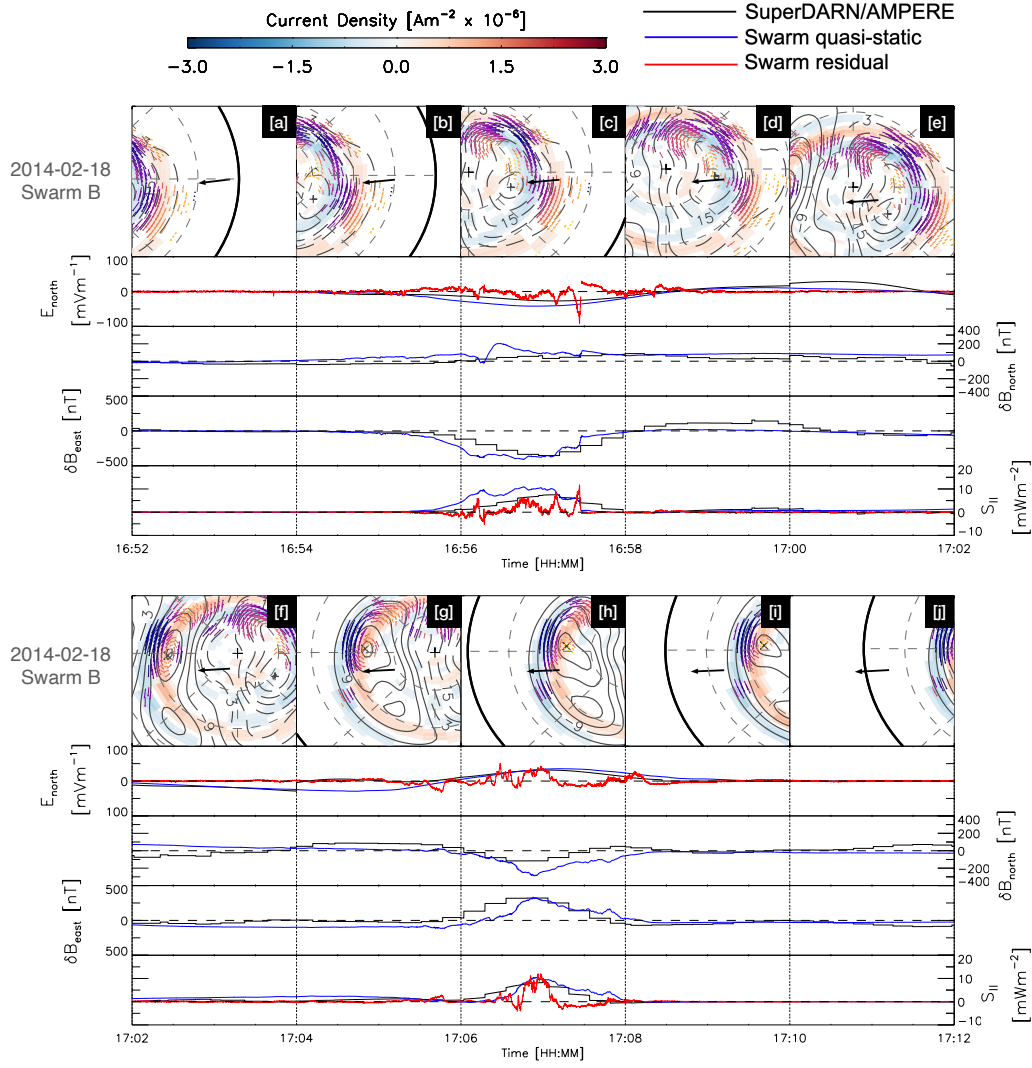


Figure 2. Swarm B-SuperDARN-AMPERE comparisons on 2014-02-18 between 16:52 and 17:12 UT. The top panels show SuperDARN electric potential contours and AMPERE FAC current densities, segmented into 2-minute intervals, with the Swarm trajectory in each overplotted with a black arrow. As in Figure 1[a], colored velocity vectors show the location of binned SuperDARN radar data. Timeseries compare electric and magnetic fields, and Poynting fluxes. The color of the timeseries lines indicates if the data was from SuperDARN or AMPERE (black), Swarm quasi-static (blue), and Swarm residual (red).

189 agreement. From the total number of events, three northern hemisphere passes of Swarm
 190 A and B were chosen to show in this letter.

3 Results and Discussion

Figure 2 shows Swarm-SuperDARN-AMPERE comparisons during a polar pass from Swarm B on 2014-02-18. The data is segmented into 2-minute intervals from which a new SuperDARN convection and AMPERE FAC pattern was generated, given at the top of each timeseries set. The black arrow shows the path of Swarm B during each segment as it bisects the plasma convection cells on the dawnside (panels a-e) and duskside (panels f-j). In panels [c] and [h] respectively, the satellite passes perpendicularly through the R1 and R2 FACs on the dawn and dusk sides. The timeseries, from top to bottom, show comparisons between northward electric fields, northward perturbation magnetic fields, eastward perturbation magnetic fields, and Poynting flux. The Kp index during this pass was low (2+).

The electric field comparisons in Figure 2 are between the SuperDARN convection (black), Swarm quasi-static (blue, $\mathbf{E}_{\text{static}}$), and Swarm residual (red, $\delta\mathbf{E}$) components. Between [a] and [e], $\mathbf{E}_{\text{static}}$ is negative (equatorward) until passing the centre of the dawn convection cell, where it turns positive (northward) along with the SuperDARN. As the direction of north and south changes as the spacecraft crosses the pole in panel [e], the sign of the SuperDARN electric field flips because the overall convection pattern orientation represents a dawn-to-dusk electric field. Swarm $\mathbf{E}_{\text{static}}$ also flips sign and matches the SuperDARN trace almost identically in panel [f], but a rapid convection pattern change in [g] in the same region causes discontinuity. This change could be because the poleward part of the dusk cell is not well constrained by radar data in panels [f] and [g]. As the dusk-side FACs are crossed however, there is once again good SuperDARN data coverage and an excellent correspondence with Swarm $\mathbf{E}_{\text{static}}$. Overall, this event illustrates that our filtering scheme for Swarm data into a quasi-static component produces a remarkable consistency with SuperDARN convection map data, when radar coverage is good.

The Swarm residual electric field is close to zero except when the satellite comes into contact with the FAC regions seen by AMPERE (Figure 2, panels c and h). In contrast to $\mathbf{E}_{\text{static}}$, $\delta\mathbf{E}$ contains a significant amount of structure and variability, both on small and mesoscales. Because of the good agreement between $\mathbf{E}_{\text{static}}$ and SuperDARN, the spatiotemporal variability in $\delta\mathbf{E}$ essentially corresponds to that which is underestimated by the SuperDARN convection map.

For the Swarm $\delta\mathbf{B}$ comparisons with AMPERE, there is an excellent correspondence in the eastward direction with clearly defined field-aligned current signatures (i.e., a westward $\delta\mathbf{B}$ deflection on the dawnside and an eastward one on the duskside). We do note however that Swarm appears to see the FACs slightly earlier in the eastward $\delta\mathbf{B}$ than AMPERE on the dawnside (panels b and c), and later on the duskside (panel h). This implies that in this case the AMPERE fit is placing the FACs slightly poleward of Swarm observations. For northward $\delta\mathbf{B}$, there is a poorer correspondence between Swarm and AMPERE which is slightly more consistent on the duskside compared to dawn.

The bottom timeseries in Figure 2 compares the Poynting flux from Swarm with that from the SuperDARN/AMPERE method. Because $\mathbf{E}_{\text{static}}$ from Swarm is well represented by the convection electric field from the SuperDARN, the quasi-static Poynting flux from Swarm and SuperDARN/AMPERE correlate well. There is however a considerable amount of Poynting flux observed by Swarm that is not captured by SuperDARN/AMPERE. Indeed, the magnitude of $\mathbf{S}_{\text{residual}}$ is comparable to $\mathbf{S}_{\text{static}}$ in the FAC regions, illustrating that as much as $\sim 50\%$ of the Poynting flux energy budget is from small and mesoscales. This large discrepancy agrees with recent work by Billett, McWilliams, Pakhotin, et al. (2022), who showed that the calculated Poynting flux decreases with increasing scale size of measurements due to increasing electric field variability. It is clear that we see multi-scale variability within $\delta\mathbf{E}$ and hence $\mathbf{S}_{\text{residual}}$, likely as a result of Alfvén waves at high frequencies (e.g., Miles et al., 2018; Pakhotin et al., 2018) and plasma instabilities/shears at lower (but not quasi-static) frequencies (Cousins & Shepherd, 2012; Cousins et al., 2013). $\mathbf{S}_{\text{static}}$ will thus largely depend on large-scale solar wind driving conditions, whilst the $\mathbf{S}_{\text{residual}}$ embedded within the quasi-static system will depend more on season and solar cycle (Matsuo & Richmond, 2008).

Figure 3 shows two events where Swarm A crossed the duskside on 2016-05-06 (panels a-e), and two days later on 2016-05-08 (panels f-j), in the same format as Figure 2. The Kp index for the 2016-05-06 event was low (2+), and for the 2016-05-08 event indicated a moderate geomagnetic storm (6-). Note that the scales are different between panels [a]-[e] and [f]-[j], particularly the Poynting flux and eastward $\delta\mathbf{B}$, which reach significantly higher magnitudes during the storm event.

For the 2016-05-06 event in Figure 3[a]-[e], there was excellent SuperDARN radar data coverage of the entire dusk convection cell. The Swarm $\mathbf{E}_{\text{static}}$ correlates very well

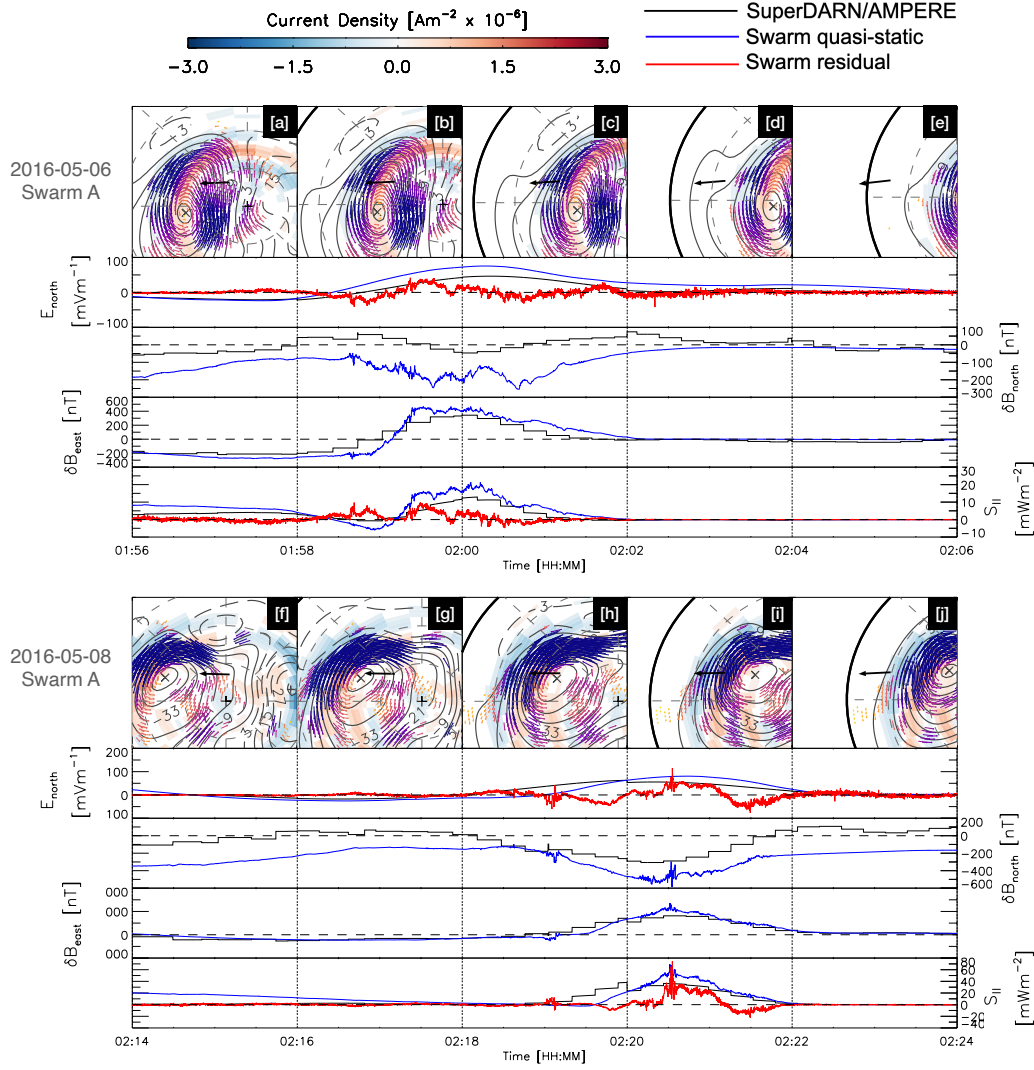


Figure 3. Same format as Figure 2, but for events on 2016-05-06 (panels a-e) and 2016-05-08 (panels f-j) with Swarm A.

with the SuperDARN convection electric field, but there is overall a higher magnitude between panels [b] and [d]. Similar to Figure 2, there is a fairly poor correlation between the Swarm northward $\delta \mathbf{B}$ and AMPERE, but a very good correlation in the eastward direction. Contrasting to the event shown in Figure 2, however, is small-scale variability within the magnetic field measurements whilst Swarm traverses the FACs in panels [b] and [c]. This $\delta \mathbf{B}$ variability is indicative of filamentary FACs embedded within the R1 and R2 currents (Neubert & Christiansen, 2003; Lukianova, 2020), which the fitted AMPERE data effectively only sees as smoothed-out and large-scale structures.

The correlation between the Swarm quasi-static and SuperDARN/AMPERE Poynting fluxes is once again very good in Figure 3[a]-[e]. Interestingly, Swarm sees a sustained 40 s period of negative (upward) $\mathbf{S}_{\text{static}}$ in panel [b], which SuperDARN/AMPERE does see, but to a much lesser degree ($\sim 6 \text{ mW m}^{-2}$ compared to $\sim 0.5 \text{ mW m}^{-2}$). Upward Poynting flux implies thermospheric forcing of the ionosphere (such as via a neutral wind flywheel) rather than the other way around, leading to electromagnetic energy transferring from the atmosphere to the magnetosphere (W. Deng et al., 1993). We also note that $\mathbf{S}_{\text{residual}}$ is positive at the same time as the negative $\mathbf{S}_{\text{static}}$, and at a similar magnitude, meaning that the total Poynting flux in that 40 s period would be much closer to zero. The balance between $\mathbf{S}_{\text{static}}$ and $\mathbf{S}_{\text{residual}}$ tells us that the thermosphere can generate large-scale quasi-static electric fields whilst effectively being “countered” by Alfvén waves and mesoscale dynamics of magnetospheric origin, an observation that would be missed by utilizing SuperDARN and AMPERE alone.

The comparisons between Swarm, SuperDARN and AMPERE remain consistent even for storm-time events, such as that shown in Figure 3[f]-[j]. The primary differences from a quieter event are the magnitudes of measurements, particularly the eastward $\delta\mathbf{B}$ and Poynting fluxes. Eastward $\delta\mathbf{B}$ ’s reach in excess of 1000 nT for Swarm and slightly less for AMPERE, whilst both $\mathbf{S}_{\text{static}}$ and $\mathbf{S}_{\text{residual}}$ reach $\sim 70 \text{ mW m}^{-2}$. The SuperDARN convection pattern and AMPERE FACs extend considerably more equatorward than the other events shown in this letter, consistent with the expanding-contracting polar cap paradigm (Cowley & Lockwood, 1992). The northward $\delta\mathbf{B}$ from AMPERE is once again significantly different from that measured by Swarm, but it does follow a similar trend, offset in magnitude.

In Figure 3[f]-[j], Swarm A traverses the duskside convection cell. We see very small-scale wave-like fluctuations in both the Swarm electric and magnetic field measurements, coincident with each other in panels [h] and [i], which propagate into $\mathbf{S}_{\text{static}}$ and $\mathbf{S}_{\text{residual}}$. The kilometre-scale sizes of these fluctuations is consistent with Alfvénic perturbations (Rother et al., 2007) occurring whilst Swarm is within the duskside FACs, similar to observations of embedded waves by Wu et al. (2020).

4 Summary

In this letter, we have made electric and magnetic field comparisons between the global scale fits of the SuperDARN and AMPERE, with high spatiotemporal resolution data from the Swarm constellation. We show that applying a Savitsky-Golay low-pass filter of 225s to the Swarm electric field data produces a smoothed component which is exceptionally close to the electric field derived from the SuperDARN convection patterns. The residual electric field from Swarm therefore comprises of fluctuations on small and mesoscales which the SuperDARN is unable to capture. Effectively, we have illustrated and validated a way of extracting the large-scale quasi-static component of the ionospheric Poynting flux from Swarm, leaving behind a residual which captures the structures embedded within.

Utilizing this new filtering scheme we examined three polar-pass events, comparing the Swarm quasi-static ($\mathbf{S}_{\text{static}}$) and residual ($\mathbf{S}_{\text{residual}}$) Poynting fluxes to those calculated using the SuperDARN and AMPERE. For all events, including a Kp 6- geomagnetic storm, the timeseries curve for $\mathbf{S}_{\text{static}}$ was very close in shape and magnitude to that derived from the SuperDARN and AMPERE. $\mathbf{S}_{\text{residual}}$, however, showed a significant amount of variability and often reached or exceeded $\mathbf{S}_{\text{static}}$. In the events we examined alone, small and mesoscale Poynting flux generators accounted for as much as half of the total magnetosphere-ionosphere electrodynamic energy budget. Thus, we expect that instruments specialised in observing large-scale ionospheric structures critically underestimate the variability and magnitude of the sub-quasi-static system.

In particular, the data comparisons in this letter reveal striking structure embedded within and between the large-scale R1 and R2 field-aligned currents, indicative of mesoscale dynamics and Alfvén waves impinging on the ionosphere. These comparisons would have not been possible were it not for the SuperDARN and AMPERE providing global-scale coverage of the high-latitude convection and field-aligned current patterns, essentially forming a comprehensive “map” so that the Swarm data could be interpreted effectively. We stress the importance of future multi-instrument comparisons such as these to help untangle multi-scale ionospheric processes.

Acknowledgments

This research was supported by the European Space Agency (ESA) Living Planet Fellowship programme and by the National Sciences and Engineering Research Council of Canada (NSERC). DDB was supported by ESA under the “HLPF-SSA” project and by NSERC under CREATE Grant #479771-20. KM was supported by NSERC Discovery Grant #RGPIN 05472-2017. SKV and the collection and processing of data for AMPERE was supported by the US National Science Foundation under AGS grant #2002574. Thermal Ion Imager (TII) data processing and calibration are supported at the University of Calgary via Canadian Space Agency Grant 15SUSWARM. The authors also acknowledge the use of data from SuperDARN, an international project made possible by the national funding agencies of Australia, Canada, China, France, Italy, Japan, South Africa, Norway, the United Kingdom and the United States of America. We also thank the AMPERE team and the AMPERE Science Center for providing the Iridium derived data products.

Open Research

16 Hz TII data from the ESA Swarm A and B satellites was obtained from <https://swarm-diss.eo.esa.int>, in the “Advanced/Plasma_Data/16_Hz_TIII_Cross-track_Dataset/New_baseline” directory. 50 Hz high-res magnetic field measurements were obtained from the “Level1b/Latest_baselines/MAGx_HR” directory. Fitted SuperDARN data can be downloaded from Globus, instructions of which are provided here: <https://superdarn.ca/data-products>. Raw SuperDARN data with DOI’s can be accessed via: <https://www.frdr-dfdr.ca/repo/collection/superdarn>. AMPERE data can be plotted and downloaded at: <http://ampere.jhuapl.edu/>.

References

- Alken, P., Thébault, E., Beggan, C. D., Amit, H., Aubert, J., Baerenzung, J., . . . others (2021). International geomagnetic reference field: the thirteenth generation. *Earth, Planets and Space*, 73(1), 1–25.
- Anderson, B. J., Angappan, R., Barik, A., Vines, S. K., Stanley, S., Bernasconi, P. N., . . . Barnes, R. J. (2021). Iridium communications satellite constellation data for study of Earth’s magnetic field. *Geochemistry, Geophysics, Geosystems*, 22(8), e2020GC009515.

- Anderson, B. J., Korth, H., Waters, C. L., Green, D. L., Merkin, V. G., Barnes,
R. J., & Dyrud, L. P. (2014). Development of large-scale Birkeland currents
determined from the Active Magnetosphere and Planetary Electrodynamics
Response Experiment. *Geophysical Research Letters*, *41*(9), 3017–3025.
- Billett, D. D., Hosokawa, K., Grocott, A., Wild, J. A., Aruliah, A. L., Ogawa, Y., ...
Lester, M. (2020). Multi-instrument observations of ion-neutral coupling in the
dayside cusp. *Geophysical Research Letters*, *47*(4), e2019GL085590.
- Billett, D. D., McWilliams, K. A., Kerr, R. B., Makela, J. J., Chartier, A. T., Ruo-
honiemi, J. M., ... Riccobono, J. (2022). Mid-latitude neutral wind responses
to sub-auroral polarization streams. In *Annales geophysicae* (Vol. 40, pp.
571–583).
- Billett, D. D., McWilliams, K. A., Pakhotin, I. P., Burchill, J. K., Knudsen, D. J.,
& Martin, C. J. (2022). High-Resolution Poynting Flux Statistics From the
Swarm Mission: How Much Is Being Underestimated at Larger Scales? *Journal of Geophysical Research: Space Physics*, *127*(7), e2022JA030573.
- Billett, D. D., McWilliams, K. A., Perry, G. W., Clausen, L. B. N., & Anderson,
B. J. (2022). Ionospheric energy input in response to changes in solar wind
driving: Statistics from the SuperDARN and AMPERE campaigns. *Journal of Geophysical Research: Space Physics*, *127*(3), e2021JA030102.
- Billett, D. D., Perry, G. W., Clausen, L. B. N., Archer, W. E., McWilliams, K. A.,
Haaland, S., ... Anderson, B. J. (2021). The relationship between large scale
thermospheric density enhancements and the spatial distribution of Poynting
flux. *Journal of Geophysical Research: Space Physics*, *126*(5), e2021JA029205.
- Burchill, J. K., & Knudsen, D. J. (2016). *EFI TII cross-track flow data release notes*.
- Burchill, J. K., & Knudsen, D. J. (2022). Swarm Thermal Ion Imager measurement
performance. *Earth, Planets and Space*, *74*(1), 1–39.
- Chulliat, A., Brown, W., Alken, P., Beggan, C., Nair, M., Cox, G., ... Panizza, M.
(2020). The US/UK world magnetic model for 2020-2025: Technical report.
- Clausen, L. B. N., Baker, J., Ruohoniemi, J. M., Milan, S. E., Coxon, J. C., Wing,
S., ... Anderson, B. J. (2013). Temporal and spatial dynamics of the regions
1 and 2 Birkeland currents during substorms. *Journal of Geophysical Research: Space Physics*, *118*(6), 3007–3016.

- 385 Clausen, L. B. N., Baker, J. B. H., Ruohoniemi, J. M., Greenwald, R. A., Thomas,
386 E. G., Shepherd, S. G., ... others (2012). Large-scale observations of a
387 subauroral polarization stream by midlatitude SuperDARN radars: Instanta-
388 neous longitudinal velocity variations. *Journal of Geophysical Research: Space*
389 *Physics*, 117(A5).
- 390 Codrescu, M. V., Fuller-Rowell, T. J., & Foster, J. C. (1995). On the importance
391 of E-field variability for Joule heating in the high-latitude thermosphere. *Geo-*
392 *physical Research Letters*, 22(17), 2393–2396.
- 393 Cousins, E. D. P., Matsuo, T., & Richmond, A. D. (2013). Mesoscale and large-
394 scale variability in high-latitude ionospheric convection: Dominant modes and
395 spatial/temporal coherence. *Journal of Geophysical Research: Space Physics*,
396 118(12), 7895–7904.
- 397 Cousins, E. D. P., & Shepherd, S. G. (2012). Statistical characteristics of small-scale
398 spatial and temporal electric field variability in the high-latitude ionosphere.
399 *Journal of Geophysical Research: Space Physics*, 117(A3).
- 400 Cowley, S. W. H., & Lockwood, M. (1992). Excitation and decay of solar wind-
401 driven flows in the magnetosphere-ionosphere system. In *Annales geophysicae*
402 (Vol. 10, pp. 103–115).
- 403 Deng, W., Killeen, T. L., Burns, A. G., Roble, R. G., Slavin, J. A., & Wharton,
404 L. E. (1993). The effects of neutral inertia on ionospheric currents in the high-
405 latitude thermosphere following a geomagnetic storm. *Journal of Geophysical*
406 *Research: Space Physics*, 98(A5), 7775–7790.
- 407 Deng, Y., & Ridley, A. J. (2007). Possible reasons for underestimating Joule heating
408 in global models: E field variability, spatial resolution, and vertical velocity.
409 *Journal of Geophysical Research: Space Physics*, 112(A9).
- 410 Dungey, J. W. (1961). Interplanetary magnetic field and the auroral zones. *Physical*
411 *Review Letters*, 6(2), 47.
- 412 Fiori, R. A. D., Koustov, A. V., Boteler, D. H., Knudsen, D. J., & Burchill, J. K.
413 (2016). Calibration and assessment of Swarm ion drift measurements using
414 a comparison with a statistical convection model. *Earth, Planets and Space*,
415 68(1), 1–17.
- 416 Fogg, A. R., Lester, M., Yeoman, T. K., Burrell, A. G., Imber, S. M., Milan, S. E.,
417 ... Anderson, B. J. (2020). An improved estimation of SuperDARN Heppner-

- 418 Maynard boundaries using AMPERE data. *Journal of Geophysical Research:*
419 *Space Physics*, 125(5), e2019JA027218.
- 420 Greenwald, R. A., Baker, K. B., Dudeney, J. R., Pinnock, M., Jones, T. B., Thomas,
421 E. C., ... others (1995). DARN/SuperDARN: A global view of the dynamics
422 of high-latitude convection. *Space Science Reviews*, 71, 761–796.
- 423 Grocott, A., Wild, J. A., Milan, S. E., & Yeoman, T. K. (2009). Superposed epoch
424 analysis of the ionospheric convection evolution during substorms: Onset lati-
425 tude dependence. In *Annales geophysicae* (Vol. 27, pp. 591–600).
- 426 Heppner, J. P., & Maynard, N. C. (1987). Empirical high-latitude electric field mod-
427 els. *Journal of Geophysical Research: Space Physics*, 92(A5), 4467–4489.
- 428 Iijima, T., & Potemra, T. A. (1976). Field-aligned currents in the dayside cusp ob-
429 served by Triad. *Journal of Geophysical Research*, 81(34), 5971–5979.
- 430 Ivarsen, M. F., Park, J., Kwak, Y.-S., Jin, Y., Knudsen, D. J., & Clausen, L. B. N.
431 (2020). Observational evidence for the role of Hall conductance in Alfvén
432 wave reflection. *Journal of Geophysical Research: Space Physics*, 125(12),
433 e2020JA028119.
- 434 Keiling, A., Thaller, S., Wygant, J., & Dombeck, J. (2019). Assessing the global
435 Alfvén wave power flow into and out of the auroral acceleration region during
436 geomagnetic storms. *Science Advances*, 5(6), eaav8411.
- 437 Knipp, D. J., Matsuo, T., Kilcommons, L., Richmond, A., Anderson, B., Korth, H.,
438 ... Parrish, N. (2014). Comparison of magnetic perturbation data from LEO
439 satellite constellations: Statistics of DMSP and AMPERE. *Space Weather*,
440 12(1), 2–23.
- 441 Knudsen, D. J., Burchill, J. K., Buchert, S. C., Eriksson, A. I., Gill, R., Wahlund,
442 J.-E., ... Moffat, B. (2017). Thermal ion imagers and Langmuir probes in
443 the Swarm electric field instruments. *Journal of Geophysical Research: Space*
444 *Physics*, 122(2), 2655–2673.
- 445 Koustov, A. V., Lavoie, D. B., Kouznetsov, A. F., Burchill, J. K., Knudsen, D., &
446 Fiori, R. A. D. (2019). A comparison of cross-track ion drift measured by the
447 Swarm satellites and plasma convection velocity measured by SuperDARN.
448 *Journal of Geophysical Research: Space Physics*, 124(6), 4710–4724.
- 449 Leger, J.-M., Bertrand, F., Jager, T., Le Prado, M., Fratter, I., & Lalaurie, J.-C.
450 (2009). Swarm absolute scalar and vector magnetometer based on helium 4

- 451 optical pumping. *Procedia Chemistry*, 1(1), 634–637.
- 452 Lomidze, L., Burchill, J. K., Knudsen, D. J., Kouznetsov, A., & Weimer, D. R.
- 453 (2019). Validity study of the Swarm horizontal cross-track ion drift velocities
- 454 in the high-latitude ionosphere. *Earth and Space Science*, 6(3), 411–432.
- 455 Lühr, H., Park, J., Gjerloev, J. W., Rauberg, J., Michaelis, I., Merayo, J. M. G., &
- 456 Brauer, P. (2015). Field-aligned currents’ scale analysis performed with the
- 457 Swarm constellation. *Geophysical Research Letters*, 42(1), 1–8.
- 458 Lukianova, R. (2020). Swarm field-aligned currents during a severe magnetic?
- 459 xmltex\break? storm of September 2017. In *Annales geophysicae* (Vol. 38, pp.
- 460 191–206).
- 461 Matsuo, T., & Richmond, A. D. (2008). Effects of high-latitude ionospheric electric
- 462 field variability on global thermospheric Joule heating and mechanical energy
- 463 transfer rate. *Journal of Geophysical Research: Space Physics*, 113(A7).
- 464 Miles, D. M., Mann, I. R., Pakhotin, I. P., Burchill, J. K., Howarth, A. D., Knud-
- 465 sen, D. J., ... Yau, A. W. (2018). Alfvénic dynamics and fine structuring of
- 466 discrete auroral arcs: Swarm and e-POP observations. *Geophysical Research*
- 467 *Letters*, 45(2), 545–555.
- 468 Neubert, T., & Christiansen, F. (2003). Small-scale, field-aligned currents at the
- 469 top-side ionosphere. *Geophysical Research Letters*, 30(19).
- 470 Pakhotin, I. P., Mann, I. R., Lysak, R. L., Knudsen, D. J., Gjerloev, J. W., Rae,
- 471 I. J., ... others (2018). Diagnosing the role of Alfvén waves in magnetosphere-
- 472 ionosphere coupling: Swarm observations of large amplitude nonstationary
- 473 magnetic perturbations during an interval of northward IMF. *Journal of*
- 474 *Geophysical Research: Space Physics*, 123(1), 326–340.
- 475 Rother, M., Schlegel, K., & Lühr, H. (2007). CHAMP observation of intense
- 476 kilometer-scale field-aligned currents, evidence for an ionospheric Alfvén res-
- 477 onator. In *Annales geophysicae* (Vol. 25, pp. 1603–1615).
- 478 Ruohoniemi, J. M., & Baker, K. B. (1998). Large-scale imaging of high-latitude con-
- 479 vection with Super Dual Auroral Radar Network HF radar observations. *Jour-*
- 480 *nal of Geophysical Research: Space Physics*, 103(A9), 20797–20811.
- 481 Ruohoniemi, J. M., & Greenwald, R. A. (1996). Statistical patterns of high-latitude
- 482 convection obtained from Goose Bay HF radar observations. *Journal of Geo-*
- 483 *physical Research: Space Physics*, 101(A10), 21743–21763.

- Senior, C., Cerisier, J.-C., Rich, F., Lester, M., & Parks, G. K. (2002). Strong sunward propagating flow bursts in the night sector during quiet solar wind conditions: SuperDARN and satellite observations. In *Annales geophysicae* (Vol. 20, pp. 771–779).
- Shepherd, S. G. (2014). Altitude-adjusted corrected geomagnetic coordinates: Definition and functional approximations. *Journal of Geophysical Research: Space Physics*, 119(9), 7501–7521.
- Sofko, G. J., Greenwald, R., & Bristow, W. (1995). Direct determination of large-scale magnetospheric field-aligned currents with SuperDARN. *Geophysical research letters*, 22(15), 2041–2044.
- Thomas, E. G., & Shepherd, S. G. (2018). Statistical patterns of ionospheric convection derived from mid-latitude, high-latitude, and polar SuperDARN HF radar observations. *Journal of Geophysical Research: Space Physics*, 123(4), 3196–3216.
- Waters, C. L., Anderson, B. J., Green, D. L., Korth, H., Barnes, R. J., & Vanhamäki, H. (2020). Science data products for AMPERE. *Ionospheric multi-spacecraft analysis tools: Approaches for deriving ionospheric parameters*, 141–165.
- Waters, C. L., Anderson, B. J., Greenwald, R. A., Barnes, R. J., & Ruohoniemi, J. M. (2004). High-latitude poynting flux from combined Iridium and SuperDARN data. In *Annales geophysicae* (Vol. 22, pp. 2861–2875).
- Waters, C. L., Anderson, B. J., & Liou, K. (2001). Estimation of global field aligned currents using the Iridium® system magnetometer data. *Geophysical Research Letters*, 28(11), 2165–2168.
- Weimer, D. R. (2001). Maps of ionospheric field-aligned currents as a function of the interplanetary magnetic field derived from Dynamics Explorer 2 data. *Journal of Geophysical Research: Space Physics*, 106(A7), 12889–12902.
- Wu, J., Knudsen, D. J., Gillies, D. M., & Burchill, J. K. (2020). Swarm survey of Alfvénic fluctuations and their relation to nightside field-aligned current and auroral arc systems. *Journal of Geophysical Research: Space Physics*, 125(3), e2019JA027220.
- Yu, Y., Cao, J., Pu, Z., Jordanova, V. K., & Ridley, A. (2022). Meso-Scale Electrodynamical Coupling of the Earth Magnetosphere-Ionosphere System. *Space Sci-*

517 *ence Reviews*, 218(8), 74.
518 Zou, S., Lyons, L. R., Wang, C.-P., Boudouridis, A., Ruohoniemi, J. M., Anderson,
519 P. C., ... Devlin, J. C. (2009). On the coupling between the Harang rever-
520 sal evolution and substorm dynamics: A synthesis of SuperDARN, DMSP,
521 and IMAGE observations. *Journal of Geophysical Research: Space Physics*,
522 114(A1).